Room-temperature quantum coherence of entangled multiexcitons in a metal-organic framework

Authors

Akio Yamauchi,[1†] Kentaro Tanaka,[1†] Masaaki Fuki,[2†] Saiya Fujiwara,[3] Nobuo Kimizuka,[1,4] Tomohiro Ryu,[5] Masaki Saigo,[5] Ken Onda,[5] Yasuhiro Kobori,*[2,6] Kiyoshi Miyata*[5] and Nobuhiro Yanai.*[1,4,7]

Affiliations

[1] Department of Applied Chemistry, Graduate School of Engineering, Kyushu University, 744 Moto-oka, Nishi-ku, Fukuoka 819-0395, Japan.

[2] Molecular Photoscience Research Center, Kobe University, 1-1, Rokkodai-cho, Nada-ku, Kobe 657-8501, Japan.

[3] RIKEN, RIKEN Center for Emergent Matter Science, Wako, Saitama 351-0198, Japan.

[4] Center for Molecular Systems (CMS), Kyushu University, 744 Moto-oka, Nishi-ku, Fukuoka 819-0395, Japan.

[5] Department of Chemistry, Graduate School of Science, Kyushu University, 744 Moto-oka, Nishi-ku, Fukuoka 819-0395, Japan.

[6] Department of Chemistry, Graduate School of Science, Kobe University, 1-1, Rokkodai-cho, Nada-ku, Kobe 657-8501, Japan.

[7] FOREST, JST, Honcho 4-1-8, Kawaguchi, Saitama 332-0012, Japan.

*Corresponding authors. E-mail: ykobori@kitty.kobe-u.ac.jp (Y.K.); kmiyata@chem.kyushu-univ.jp (K.M.); yanai@mail.cstm.kyushu-u.ac.jp (N.Y.)

[†]These authors contributed equally to this work.

Abstract

Singlet fission (SF) can generate an exchange-coupled quintet triplet pair state ^{5}TT, which could lead to the realization of quantum computing and quantum sensing using entangled multiple qubits even at room temperature. However, the observation of the quantum coherence of ^{5}TT has been limited to cryogenic temperatures, and the fundamental question is what kind of material design will enable its room-temperature quantum coherence. Here we show that the quantum coherence of SF-derived ^{5}TT in a chromophore-integrated metal-organic framework (MOF) can be over hundred nanoseconds at room temperature. The subtle motion of the chromophores in the MOF leads to the enough fluctuation of the exchange interaction necessary for ^{5}TT generation, but at the same time does not cause severe ^{5}TT decoherence. Furthermore, the phase and amplitude of quantum beating can be controlled by molecular motion, opening the way to room-temperature molecular quantum computing based on multiple quantum gate control.

Introduction

We are currently experiencing a second quantum revolution. Quantum information science (QIS) utilizes the principles of quantum mechanics for various applications such as quantum computing (*1, 2*), quantum communication (*3, 4*), and quantum sensing (*5-7*). The most basic information unit in QIS is a quantum bit (qubit). Among various types of qubit, those using molecular materials generally have the following advantages: the ability to precisely create a specific qubit structure, the ability to control qubit properties by changing the chemical structure, and the scalability to integrate many qubits (*8-10*). While most qubits require cryogenic temperatures, some molecular qubits can be initialized by photoexcitation (*11, 12*), making them particularly promising for quantum computing at room temperature and quantum sensing of living systems.

Among the photogenerated molecular qubits, singlet fission (SF) has the unique feature of being able to generate high-spin quintet state, which is useful for advanced logic gate operations and entanglement-enhanced sensing (*13-19*). SF is a process in which two triplet excitons (T_1) are generated from one photoexcited singlet (S_1), and has been studied mainly in the energy field to improve the efficiency of solar cells (*20-22*). On the other hand, many studies on the mechanism of SF have revealed that the triplet pair with singlet multiplicity ^{1}TT, in which two T_1 are strongly coupled by an exchange interaction (J), arises from S_1, and the following spin evolution of the triplet pair leads to the formation of a four-spin entangled quintet multiexciton ^{5}TT (*14-19*). SF-derived ^{5}TT can play an important role in the future development of molecular quantum computing using multiple qubits such as CNOT gate operation. ^{5}TT can not only be generated by light, but also be detected by light through the inverse process of SF, triplet-triplet annihilation (TTA), and thus has the potential to be addressed in a single spin level (*14*).

To maximize the potential of these SF-derived ^{5}TT as qubits, it is crucial to generate quantum coherence at room temperature. However, only a few cases of ^{5}TT quantum coherence have been observed so far, and these cases are limited to cryogenic temperatures of 75 K or lower (*13-15*). This poses a major challenge for the development of SF-derived ^{5}TT qubits. Most of the reported examples are based on molecular crystals of tetracene derivatives, where the two triplet excitons move apart, weakening the exchange interaction J and causing mixing between ^{1}TT and ^{5}TT, and then the triplets come close to each other again, producing a strongly exchange-coupled ^{5}TT. In this mechanism, delicate control of molecular packing is required to make the interaction between chromophores strong enough to cause SF but weak enough to suppress the triplet diffusion (*14*). Especially at room temperature, the triplet diffusion is so pronounced that the ^{5}TT pairs quickly dissociate to form non-correlated T+T states, and no coherence can be observed (*13*).

Another mechanism for SF-based ^{5}TT generation is the modulation of exchange interactions between chromophores by molecular motion, causing the conversion of ^{1}TT to ^{5}TT (*16-18*). Such a conformational change does not occur in dense molecular crystals, but has been observed in intramolecular SF systems consisting of discrete molecules of covalently linked acene units dispersed in a low-temperature glass matrix. However, while molecular motion is necessary for the generation of ^{5}TT, decoherence may be induced by fluctuations in the zero-field splitting interaction. In other words, it remains unclear what kind of molecular motion can simultaneously achieve efficient ^{5}TT generation and noise-suppressed qubits.

Here we report the first room-temperature observation of the quantum coherence of SF-derived ^{5}TT by controlling the molecular motion in a metal-organic framework (MOF).

MOFs are nanoporous crystalline materials composed of metal ions and organic ligands (*23-30*). By integrating chromophores into the ligand, the distance and angle between chromophores can be precisely regulated in MOFs (*24-26*). Unlike dense molecular crystals, MOFs have nanoscale voids in the crystals, which allow the chromophores to move, and this movement can be controlled by the topology of the network and the local molecular density around the chromophores. As a proof-of-concept, we prepare a UiO-type (*30*) pentacene-based MOF (Pn-MOF), which is synthesized by combining diamagnetic Zr ions with a dicarboxylate ligand containing pentacene (*31-33*), the most representative chromophore exhibiting exothermic SF. Note that this Pn-MOF is the first example of a MOF exhibiting SF to the best of our knowledge. The non-interpenetrated UiO-type structure can prevent π-stacking between pentacene planes, which gives the pentacene units enough motion to make the conversion from ^{1}TT to ^{5}TT (Figure 1). The dense integration in the Pn-MOF makes the pentacene motion sufficiently suppressive that the quantum coherence of ^{5}TT generated by microwave irradiation was observed for over hundred nanoseconds even at room temperature. Furthermore, the phase and amplitude of quantum beating can be manipulated by controlling molecular motion. These results reveal how molecular motions should be designed to achieve quantum coherence of multilevel distinct quantum systems, referred to as qudits, even at room temperature. This provides a fundamental guideline for the future development of molecular-based QIS.

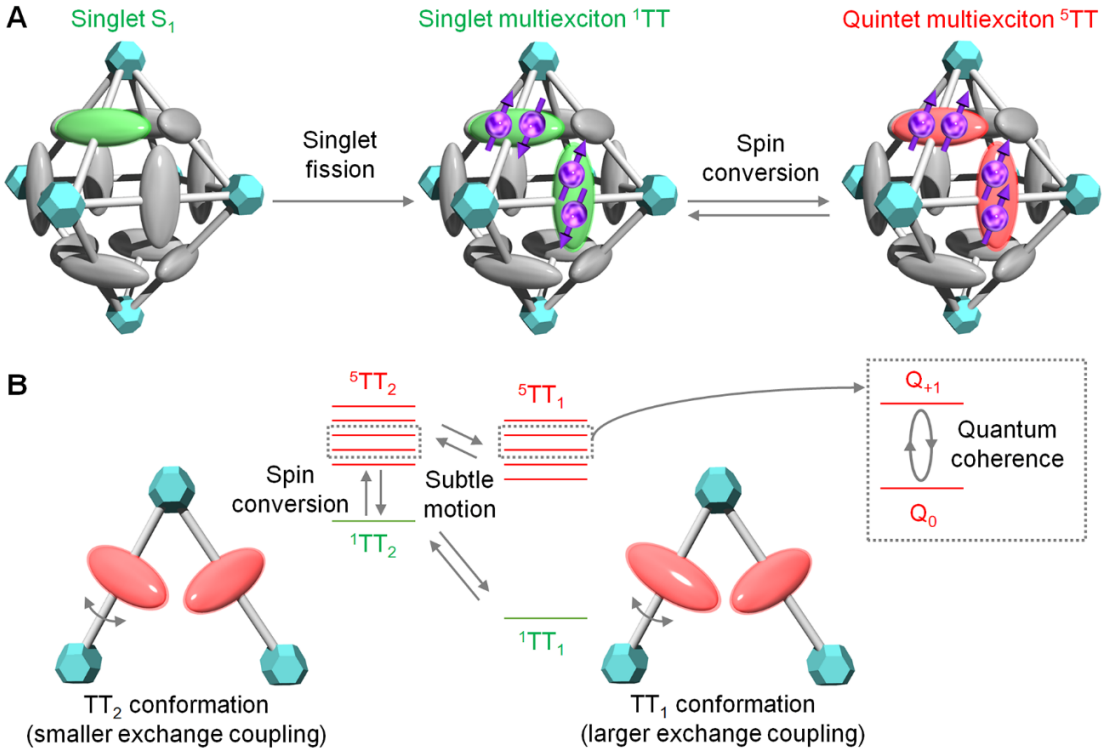

Fig. 1. Quintet multiexciton generation and its quantum coherence in a MOF. (**A**) Singlet fission (SF) followed by spin evolution via modulation of exchange interactions results in the formation of quintet multiexciton ^{5}TT in a MOF. (**B**) Suppressed chromophore motion in a MOF enables not only the spin conversion from ^{1}TT to ^{5}TT but also the quantum coherence of ^{5}TT over hundred nanoseconds even at room temperature.

Results

As a dicarboxylate ligand containing a pentacene moiety, we employed 4,4'-(pentacene-6,13-diyl)dibenzoic acid (PDBA, Fig. 2A), which we had previously developed for other purposes (*29, 34*). The energy levels of excited states of PDBA were

estimated from time-dependent density functional theory (TD-DFT) calculations. B3LYP/6-31G (d,p) and ωB97X/6-31G (d,p) were used from the ground state optimization and excited state calculations, respectively. It was confirmed that PDBA has the similar S_1 (2.34 eV) and T_1 (0.93 eV) energy levels compared with those of pentacene (S_1: 2.45 eV, T_1: 0.89 eV) (*35*), and exothermic SF is expected to occur for PDBA as well. Indeed, we have previously confirmed that aggregates of PDBA in water exhibit SF (*34*). Pn-MOF with pentacene integrated in a UiO-type structure was synthesized by a hydrothermal method using $ZrCl_4$ and PDBA in the presence of acetic acid as the modulator in deaerated DMF at 403 K. The coordination of the carboxylic acid of PDBA to the Zr-based cluster was confirmed by the shift to lower wavenumber of the peak originating from carbonyl stretching from 1685 cm^{-1} to 1595 cm^{-1} (asymmetric) and 1540 cm^{-1} (symmetric) (Fig. S1) (*36*). The structure of Pn-MOF was confirmed by powder X-ray diffraction (PXRD) measurements. The peak positions of the experimental PXRD pattern of Pn-MOF matches well with those of the simulated pattern (Fig. 2B). The simulated structure with UiO-68 type topology using PDBA as a ligand is shown in Fig. 2D. The center-to-center distance between the nearest pentacene moieties is 1 nm and the dihedral angle is 120 degrees. The distance between the nearest carbons of the nearest pentacene pair is 0.35 nm, which is close enough for SF to occur. The distance between the second nearest pentacene sites is 1.5 nm and the dihedral angle is 90 degrees. The relatively broad PXRD peaks of Pn-MOF suggest that the structure is partially disordered (*37*). In Pn-MOF, pentacene moieties do not form π-stacking with each other, which is expected to suppress immediate deactivation of triplet dimer by triplet-triplet annihilation (TTA) and to fluctuate the exchange interaction by changing the dihedral angle between pentacene units. Such moderate inter-pentacene interactions were also confirmed by UV-visible absorption measurements (Fig. 2C). The 0-0 absorption peak of the π-π* transition of the pentacene moiety was located at 602 nm in DMF solution of PDBA, while the absorption peak of Pn-MOF showed a slight broadening and red-shift to 612 nm, indicating the presence of excitonic interactions between the pentacene moieties. On the other hand, in the neat PDBA solid, the absorption peak was located at a longer wavelength of 622 nm with more broadening. This indicates that the interaction is properly controlled in Pn-MOF by preventing π-stacking between pentacene moieties.

From thermogravimetric analysis (TGA), it was found that Pn-MOF has high thermal stability up to about 573 K and also adsorbs water from the air into its nanopores (Fig. S2). The existence of nanopores in Pn-MOF was also confirmed by nitrogen gas adsorption measurements at 77 K after activation of Pn-MOF at 373 K under vacuum (Fig. S3). The adsorption isotherm of Pn-MOF showed a steep rise in the low-pressure region, which is typical for microporous materials and classified as IUPAC type I. Gradual rise was also observed in the high-pressure region, implying the broad distribution of the pore sizes and the existence of defects. Once the nanoporous structure of Pn-MOF was confirmed, Pn-MOF was soaked in paraffin. Paraffin is non-volatile, useful for dispersing MOF solids, and is sometimes used for time-resolved transient EPR measurements as an inert matrix. The PXRD pattern of activated Pn-MOF soaked in paraffin retained the original peaks, indicating that the UiO-68 type topology was preserved (Fig. 2B). The UV-Vis absorption peak shift of Pn-MOF was very small (612 nm to 615 nm) before and after the paraffin soaking (Fig. 2C). Therefore, it is likely that paraffin in the MOF nanopores does not have any strong interactions with chromophores, and inter-chromophore interactions were not affected by the introduction of guest paraffin molecules.

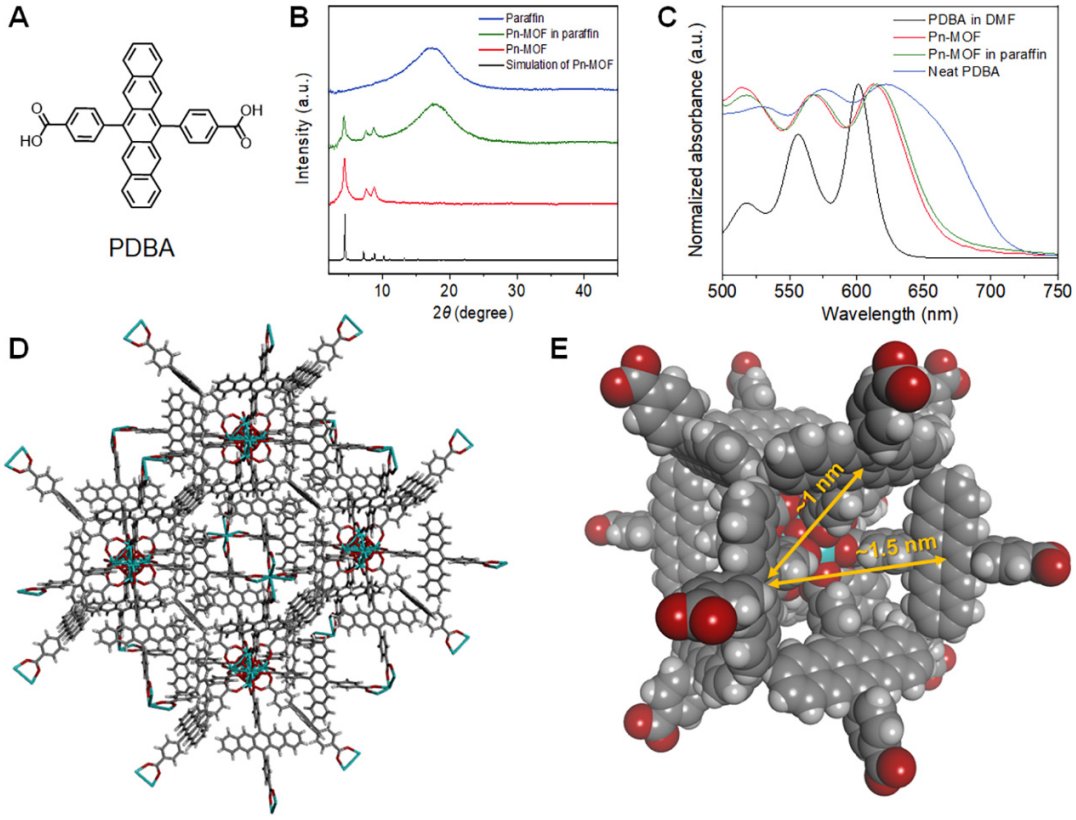

Fig. 2. Characterizations of Pn-MOF. (**A**) Chemical structure of PDBA. (**B**) Simulated PXRD pattern of Pn-MOF (black line) and experimental PXRD patterns of Pn-MOF (red line), Pn-MOF in paraffin (green line), and paraffin (blue line). (**C**) UV-vis absorption spectra of 1 mM PDBA in DMF (black line), Pn-MOF (red line), neat PDBA solid (blue line), and Pn-MOF in paraffin (green line). (**D**) Simulated structure of Pn-MOF with UiO-68 type topology. (**E**) The nearest and second nearest pentacene moieties in Pn-MOF.

Singlet fission in Pn-MOF

To investigate the singlet fission (SF) dynamics in Pn-MOF in paraffin, we carried out pump-probe type transient absorption spectroscopy (TAS) in the 460-550 nm range (Fig. 3), commonly employed for tracking SF dynamics in pentacene-based systems. Upon excitation by an ultrashort pump pulse at 600 nm, we observed a broad transient absorption spectrum around 450-500 nm, typically attributed to the feature of S_1-S_n absorption of pentacene chromophore. The spectrum subsequently transformed to a different shape with a peak at 530 nm within a hundred picoseconds (Fig. 3A, B). Since the signal at 530 nm is indicative of T_1-T_n absorption of pentacene chromophore (*38, 39*), we confirmed the ultrafast generation of the triplet pair state through SF. We can assign the second component as the triplet-pair state with singlet multiplicity, ^{1}TT, because the spin multiplicity is conserved in the ultrafast timescale. We performed global analysis assuming a sequential model with two components to analyze time constants and spectral features (Fig. 3B, C). The first and second components of the evolution-associated spectra (EAS) can reasonably be assigned from their shapes to the spectra from S_1 and ^{1}TT, respectively. The S_1 state was converted to the ^{1}TT state with a time constant of 16.8$\pm$ 0.1 ps, followed by negligible decay (>1 ns) in the current time window. The time scale of transition was slower than the typical timescale of SF in pentacene crystal (~100 fs), but still much quicker than the time scale of the typical intersystem crossing of pentacene in

solution (> 1 ns). This is consistent with successful fine control of moderate intermolecular interaction required for efficient ^{5}TT generation.

We then investigated the kinetics of the triplet pair state via nsTA in the Pn-MOF (Fig. 3D, red), which is crucial for QIS. Although the spectral shape was almost constant over time (Fig. S4), multi-component decay profile was observed. This complex kinetics suggests alternating spin multiplicity via interaction fluctuation impacts the deactivation of the triplet pair state. To confirm the origin of the multiple decays, we performed low-temperature (150 K) measurements (Fig. 3D, green), which clearly revealed slowed-down dynamics in the ns timescale without altering the spectral shape (Fig. S4), providing compelling evidence of the role of conformational fluctuation in the electron-spin coupled dynamics.

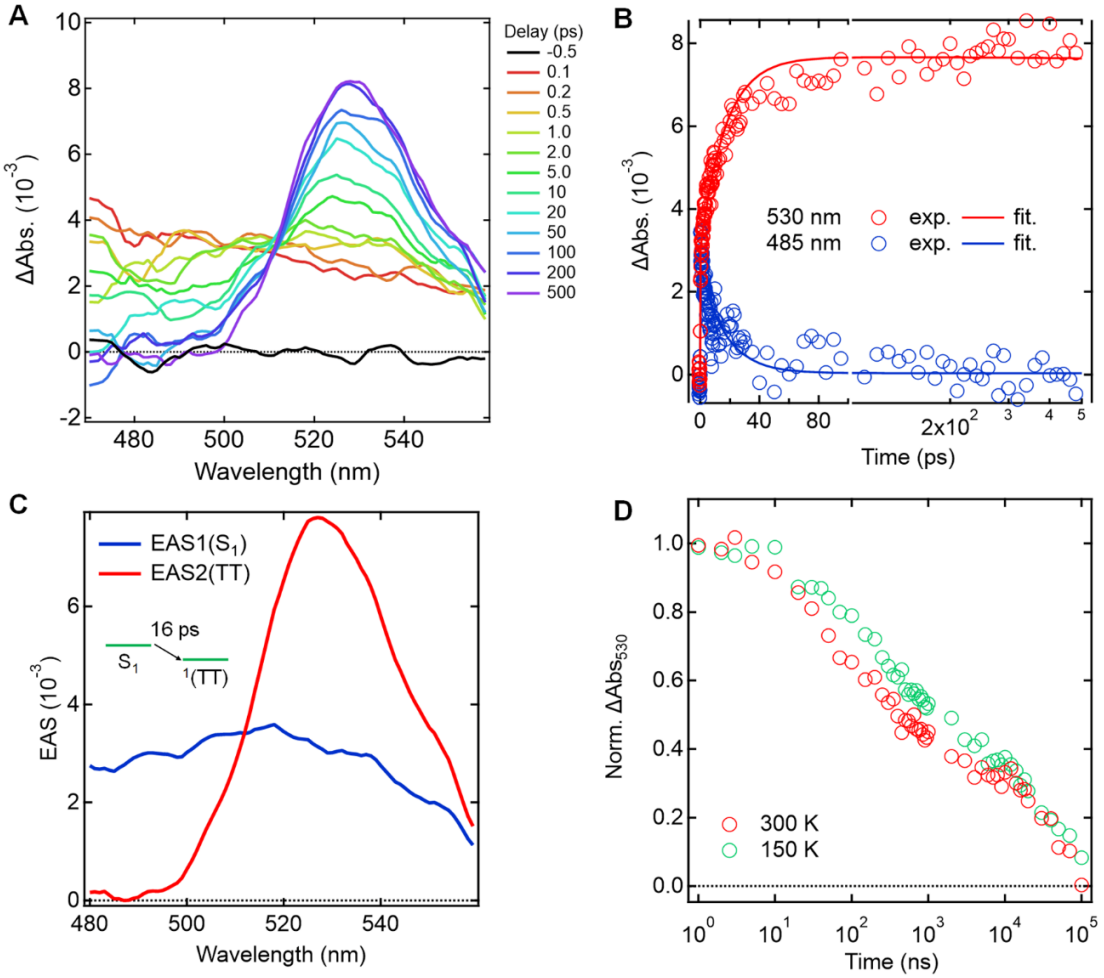

Fig. 3. **Transient absorption spectra (TAS) measurements of Pn-MOF.** (**A**) Experimentally observed spectral evolution of the fs-TAS (excitation wavelength: 600 nm) of Pn-MOF in paraffin. (**B**) Temporal change of transient absorption at selected wavelengths and fitting curves from global analysis. (**C**) Evolution associated spectra (EAS) obtained from global analysis based on the sequential models. EAS1 and EAS2 indicate the first and second components of EAS, respectively. (**D**) Temperature dependence of the transient absorption at 530 nm of Pn-MOF.

Quintet multiexciton formation in Pn-MOF

To quantitatively explore the spin dynamics in Pn-MOF, continuous-wave time-resolved electron paramagnetic resonance (CW-TREPR) measurements of Pn-MOF in

paraffin were performed at room temperature. Spin polarization signals with typical A/A/E/A/E/E pattern of quintet (A and E represent microwave absorption and emission, respectively) and E/A pattern of triplet were observed on inner and outer side of the spectra, respectively (Fig. 4A).

As mentioned above with the fs-TAS data, the EPR silent ^{1}TT state should be initially populated by SF. The spin conversion from ^{1}TT to ^{5}TT has been explained by the modulation of spin-spin exchange coupling J with a conformational change in the covalently linked chromophore dimers. In this case, the chromophores remain strongly coupled to each other even though the conformation of the dimer changes. In contrast, in dense organic crystals, triplet hopping forms weakly coupled triplet pairs, and mixing occurs between ^{1}TT and ^{5}TT, which are close to each other in energy level. The triplets then re-encounter to produce a strongly coupled ^{5}TT. The MOF in this work is a unique system that combines the characteristics of both dimers and crystals, because it has a structure in which many chromophores are accumulated, but also has nanopores inside the crystal, which allows the chromophores to rotate and change their interactions. Therefore, it is appropriate to analyze the system using a model that assumes both J-modulation in the strongly coupled TT pair and spin mixing in the weakly coupled TT pair (Scheme 1).

The ^{5}TT formation by the modulation of J through the chromophore rotations within the strongly coupled triplet pair in the 1 nm separated nearest pair shown in Fig. 2E (Scheme 1A) competes with the initial exciton migration to form the separated multiexcitons (Scheme 1B and 1C). Depending on local exciton mobility by crystallinity or disorder, the weakly coupled triplet pair (Scheme 1B) and the non-correlated two triplets T+T (Scheme 1C) can separately be generated by the exciton migration. The quick triplet exciton dissociation at the crystalline domain would preferentially produce well-separated non-correlated T+T and does not contribute to the electron spin polarization. In contrast, the weakly coupled triplet pair states are anticipated to be generated at the disorder region of the MOF to form the spin correlated triplet pair (SCTP) (T+T) causing the nine adiabatic states (|1>, |2>, ⋯ and |9>) by quantum superpositions of the nine of singlet, triplet and quintet diabatic characters, as shown in Scheme 1B. These SCTP contributions are observed at the peak positions of the outermost magnetic fields (298 and 343 mT) exhibiting the E/A spin polarization pattern in Fig. 4A by the spin-spin exchange coupling of J = 1 mT in the 1.5 nm separated exciton pair (Fig. 2E).

From Scheme 1, we computed time-development of the singlet, triplet and quintet diabatic characters for the three different exciton-pair conformations (TT_1, TT_2, and weakly coupled (T+T)) together with the different J values to reproduce the time-dependent EPR data using the density matrix formalism analysis (Table S1). The EPR spectra were simulated as shown by the red lines in Fig. 4A. The electron spin polarization pattern (A/A/E/A/E/E) in the quintet is sensitive to the mutual orientations of the excitons in the TT and are generated by fluctuation of the exchange coupling. From the simulation of the EPR spectra, we obtained the dihedral angle (β = 130 degrees) between the aromatic planes in TT_1 as shown in Fig. 4B. β = 150 degrees is obtained for the T_B moiety in the TT_2 state as imposed in Fig. 4B, denoting that the conformation changes by molecular rotations (red arrows in Fig. 4B) are coupled to the modulation of the exchange interaction in Table S1. The stronger J (= -1.4×10^5 MHz) in the TT_1 than that (J = -1.9×10^4 MHz) in the TT_2 is consistent with the dimer model geometry of TT_1 and TT_2 causing contact edge-to-edge separations (0.29 nm and 0.30 nm, respectively) between carbon atoms in the Pn moieties in Fig. 4B based on the simulated structure (Fig. 2E). This supports the molecular rotation along with the Pn-ligating direction for the J-modulation.

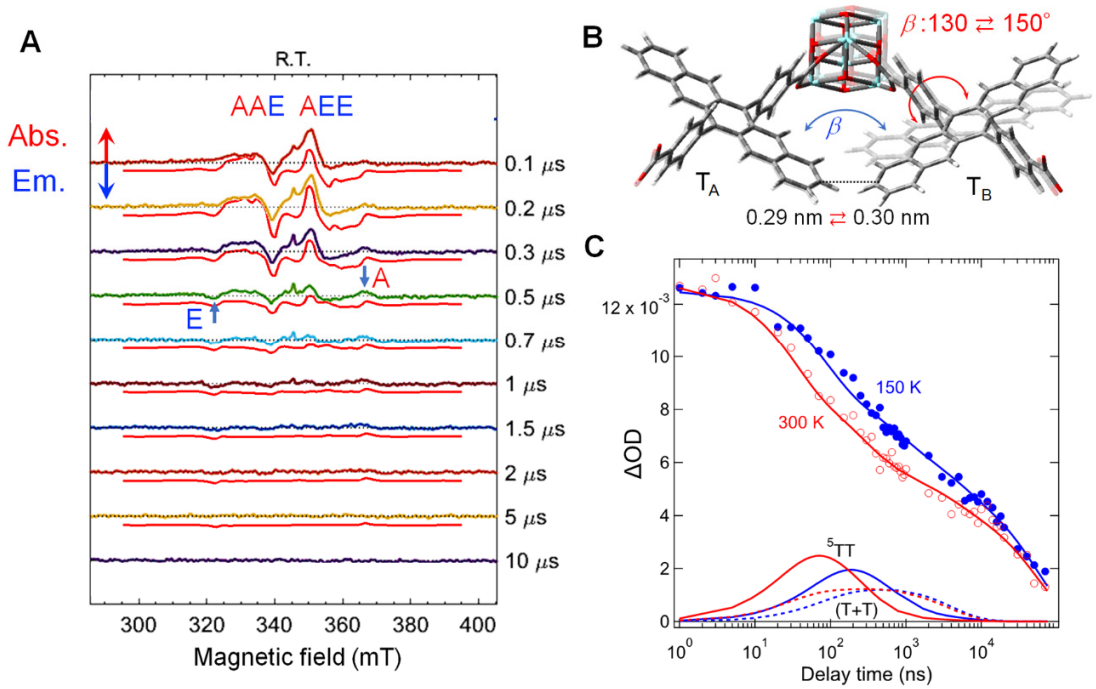

Fig. 4. **Transient EPR spectra of Pn-MOF.** (**A**) TREPR spectra for different delay times of Pn-MOF in paraffin at room temperature. Spectrum simulations by the rotation model analysis in Scheme 1 are shown under the experimental data (red lines). (**B**) Conformations of the quintet TT_1 and TT_2. The blue arrow represents dihedral angle (β) of the aromatic plane in T_B relative to T_A in the T_AT_B pair. (**C**) Decay profiles of the absorbance changes in ns-TAS (ΔOD) by the multiexcitons at temperatures of 300 K (red circles) and 150 K (blue circles), together with simulated profiles by the rotation model analysis (red and blue lines). Contributions of ^{5}TT and SCTP (T+T) are shown by the solid and dashed lines, respectively, at 300 K (red line) and 150 K (blue line).

Scheme 1. **Model of the density matrix formalism analysis.** Different multiexcitons, (**A**) strongly coupled triplet pair ^{5}TT ($^5TT_1$ and $^5TT_2$), (**B**) weakly coupled spin correlated triplet pair (T+T), and (**C**) non-correlated two triplets T+T, are included with considering molecular rotation, exciton migration and reencounter processes.

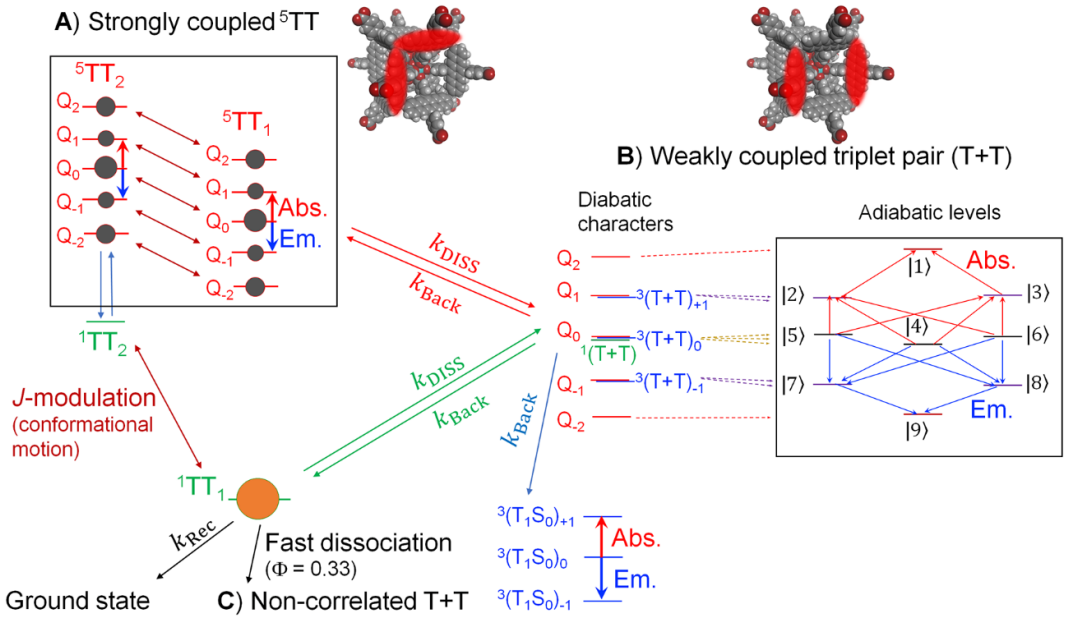

As a result, the time evolution of the EPR spectra were successfully reproduced by the model of Scheme 1 in which the hopping-dissociation (k_{DISS}) and re-encounter (k_{Back}) to form the quintet ^{5}TT, triplet $^3(T_1S_0)$, and singlet ^{1}TT via triplet-triplet annihilation of $^3(T+T)_0$ are considered together with the *J*-modulation between TT_1 and TT_2 to generate the anisotropy in the quintet sublevel populations (Figure 4A, red lines). This analysis was also applied to understand the time development of the transient absorption signals in paraffin for $t \geq 1$ ns in the absence of the magnetic field. Notably, the profiles (solid lines in Fig. 4C) of the sum of the triplet excitons ($^5TT_1 + {}^5TT_2 + {}^3T_1S_0 + {}^1TT_1 + {}^1TT_2$ + SCTP (T+T) + non-correlated T+T) are consistent with the deactivation kinetics of the spin-polarized exciton pairs with ^{5}TT and (T+T) in Fig. 4A. Quick nanoseconds decays in Fig. 4C are originating from the singlet deactivation process ($k_{Rec} = 5.6\times10^7$ s^{-1} at room temperature) of ^{1}TT that is in equilibrium with ^{5}TT and (T+T). The longer-lived transient absorption profile at 150 K than at 300 K is due to slower singlet deactivation ($k_{Rec} = 2.0 \times10^7$ s^{-1}). Longer lived multiexciton EPR signals are also obtained at 150 K (Fig. S5).

Room-temperature coherence control of quintet state

To directly control the four spin qubits of the quintet multiexciton at room temperature, we applied a transient nutation microwave pulse sequence using an X-band pulsed EPR spectroscopy (Fig. 5A and 5B). Although the quintet states are significantly minor at the later delay time exceeding 1 μs in Fig. 4A and 4C because of the quick deactivation in the strongly coupled TT pair to the ground state, interestingly, the echo detected EPR spectrum of the quintet is observed even at $\tau_{delay} = 1.1$ μs (Fig. 5C). This suggests that some of the strongly coupled TT states exist as minor traps while other dominant TT states undergo quick deactivation and dissociation by hot exciton characters with relatively large angular molecular rotation shown in Fig. 4B. Such hot multiexcitons should also be subject to significant transverse spin relaxation and not contribute to the echo signal. At the field strength of $B_0 = 348.1$ mT (blue arrow in Fig. 5C), we obtained the microwave-induced spin coherence of the quintet as shown in Fig. 5E. This profile is successively explained by the superpositions of the nutation frequencies (ω_{m_S}) contributed by the quintet quantum gates of $\Delta m_s = \pm1$ in Fig. 5B (Scheme 1A) described by the following equation,

$$\omega_{m_S} = \frac{g\mu_B B_1}{\hbar}\sqrt{S(S+1) - m_S(m_S \pm 1)} \qquad (1)$$

where m_s (= 0, ±1, and ±2) represent the quintet sublevel quantum numbers causing the transitions of $\Delta m_s = \pm1$ with $S = 2$ in Scheme 1A (detailed analysis method is described in Table S2). A decoherence time constant of $T_{2D} = 150$ ns is employed. This is consistent with the transverse relaxation time of $T_2 = 122$ ns in Fig. S6D. B_1 is the microwave field strength in eq.(1) and is set to be $B_1 = 0.45$ mT. The nutation frequency varies with the quantum gate: $\omega_{m_S} = \sqrt{6}\, g\mu_B B_1/\hbar$ for the gates ($Q_{0,\pm1}$) between Q_0 and $Q_{\pm1}$ and $\omega_{m_S} = 2g\mu_B B_1/\hbar$ for the gates ($Q_{\pm2,\pm1}$) between $Q_{\pm2}$ and $Q_{\pm1}$. Therefore, anisotropic quintet sublevel distribution by the S-Q_{mS} interconversion in Scheme 1A highly influences the frequencies and amplitudes of the quantum beats induced by the coherent microwave pulses at a field strength of B_0. The quantum beat profile is well reproduced by the dynamic model of the quintet populations considering subtle conformational motion between the dihedral angles of $\beta = 130$ degrees and 122 degrees in the T_AT_B exciton pair for TT_1 and TT_2, respectively, which causes the fluctuation in the through-space separations between 0.29 and 0.32 nm (Figs. 5D and 5E). In the simulated profile (red

lines in Fig. 5E and 5F) a minor lower frequency component (green line in Fig. 5E) is included by the gates between $Q_{\pm 2}$ and $Q_{\pm 1}$, denoting that the two different nutation frequencies of 25 and 31 MHz are involved with opposite polarizations (Fig. 5B) in the experimental profile. The larger dihedral motion between β = 130 degrees and 150 degrees in Fig. 4B however causes the deviated nutation profile (green dashed line in Fig. 5F) from the experimental result, supporting that the minor traps with the smaller angular motions (β = 130 degrees and 122 degrees, Fig. 5D) are the origin of the quintet state showing long lifetime and over hundred nanoseconds of spin coherence.

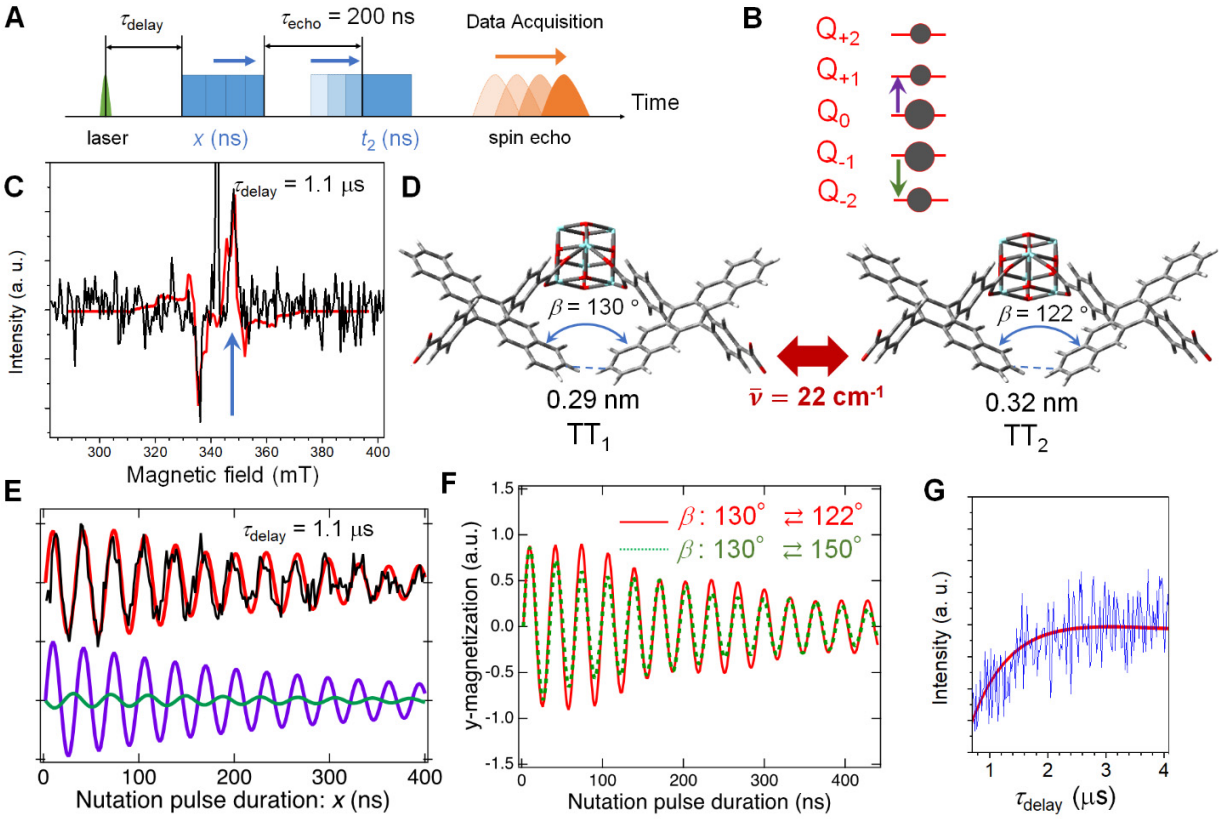

Fig. 5. **Transient nutation of the quintet state at room temperature.** (**A**) Pulse sequence of the transient nutation measurement. (**B**) Two main quantum gates detected by the pulsed microwave at B_0 = 348.1 mT in the quintet sublevels. (**C**) Echo detected EPR spectrum at τ_{delay} = 1.1 μs. The durations of the first and second pulses are x = 8 ns and t_2 = 16 ns, respectively. Fitting result using eq. S1 and Table S2 is shown as a red line. (**D**) Molecular model of the TT-state conformation motions at a frequency of $\bar{\nu}_{vib}$= 22 cm^{-1} that explains anisotropy of the sublevel populations in (**B**). (**E**) Transient nutation profiles as a function of x in (**A**) at τ_{delay} = 1.1 μs using t_2 = 16 ns. The simulated profile is shown by a red line considering the anisotropic sublevel populations. At the bottom, decomposition of the computed nutation data by the gates $Q_{0,\pm 1}$ and $Q_{\pm 2,\pm 1}$ are shown by purple and green lines, respectively. (**F**) Simulated profiles by the different rotation models. The red solid line corresponding to the red line in (**E**) is computed by the conformation motion between the dihedral angles of β = 130 degrees and 122 degrees of the T_B molecule in the T_AT_B pair for TT_1 and TT_2, respectively. Green dotted line is obtained with considering the large dihedral angle change between β = 130 degrees and 150 degrees in Fig. 4B. (**G**) Dependence of τ_{delay} on the echo intensity employing x = 16 ns, t_2 = 32 ns and τ_{echo} = 184 ns with B_1 = 0.70 mT. Fitting result using eq. S1 and Table S2 is shown as a red line.

Specifically, the limited dihedral angle fluctuation in β (Fig. 5D) is revealed to result in amplitude enhancement of the transverse magnetization by the gate of $Q_{0,1}$ (purple in Fig. 5B and 5E) at B_0 = 348.1 mT from Fig. S7A, while the magnetization cancellation occurs in total by the $Q_{0,\pm1}$ gates for the larger angle-fluctuation case in Fig. S7B. The hindered rotation thus leads to dominant amplitude of the high-frequency nutation component at 31 MHz in Fig. 5E (purple) determined by $\omega_0 = \sqrt{6}\, g\mu_B B_1/\hbar$ (the absorptive gate in Fig. 5B) by summing the anisotropic spin polarization, giving rise to the minor lower frequency nutation contribution (25 MHz, green wave in **E**) by $\omega_{-2} = 2g\mu_B B_1/\hbar$ (green emissive arrow in Fig. 5B) participating to the quantum beat. This is also consistent with the echo-detected EPR spectrum (red line in Fig. 5C) obtained using this rotation model. These results imply that the quantum beating behavior can be controlled by the degree of the structural fluctuation.

Discussion

For quintet multiple excitons generated by photo-induced SF, it has been unclear what kind of molecular motion is required to achieve both 1) effective quintet generation and 2) noise suppressed qubits. Conformational motion is necessary for the spin conversion from ^{1}TT to ^{5}TT. However, if the change in orientation angle of the chromophore relative to the magnetic field is too large, not only does exciton hopping cause dissociation and recombination between excitons, but also ^{5}TT quantum decoherence occurs, making it impossible to use as a qubit. On the other hand, low-mobility triplet pairs with small orientation angle changes prevent exciton hopping and recombination. In addition, and importantly, the suppression of transverse relaxation due to fluctuations in the zero-field splitting interaction makes it possible to slow down decoherence and function as qubits even at room temperature.

To explicitly understand this trap characteristic for manipulation of the microwave-induced spin coherences, we plotted the echo intensity at 348.1 mT as a function of the delay time (τ_{delay}) (Fig. 5G). The decay time (1.0 μs) of the echo signal of the quintet is much longer than the decay time (0.2 μs) of the quintet signals (Fig. 4) detected by the CW-TREPR and TAS methods and is well fitted by the rotation model calculations (red lines in Figs. 5C and 5G) using $k_{Rec} = 1.1\times10^7$ s^{-1} at room temperature (Table S2), demonstrating that the minor trap quintet species are only responsible for the quantum coherence. Such room-temperature ^{5}TT quantum coherence based on control of chromophore motion in MOFs is in contrast to previous ^{5}TT generation based on exciton diffusion in dense molecular crystals, which is not immune to triplet separation and decoherence at room temperature. The usefulness of ^{5}TT as qubits has been demonstrated at cryogenic temperatures, but control of molecular motion in MOFs leads to room temperature drive of ^{5}TT qubits.

We revealed that the chromophore motion controls the phase and amplitude of the frequency component of its quantum beating. Such control of multiple quantum gates is also extremely important for future developments in molecular quantum computing with multiple qubits, such as verification of CNOT gates.

It is significant that not only the generation of quantum coherence by microwave irradiation has been demonstrated at room temperature by controlling chromophore motion in a MOF, but also the details of molecular motion (change in molecular orientation) that enable the realization of room-temperature qubits have been discovered. In the present system, the low-mobility part that can generate ^{5}TT coherence is only a part

of the MOF. It will be possible to generate ^{5}TT qubits more efficiently in the future by searching for guest molecules that can induce more such suppressed motions and by developing suitable MOF structures. Precise control of the assembly structure and motion of the chromophores in MOFs is expected to lead to the development of innovative materials useful for the molecular-based QIS.

Materials and Methods

All reagents were used as received unless otherwise noted. Dry THF was prepared by treating with Molecular Sieves 4A 1/8, Wako. Liquid paraffin, *n*-butyl lithium in hexane and zirconium tetrachloride ($ZrCl_4$) were purchased from Sigma-Aldrich. *p*-Toluene sulfonic acid, tin(II) chloride dihydrate ($SnCl_2{\cdot}2H_2O$), sodium chlorite ($NaClO_2$), sodium dihydrogen phosphate (NaH_2PO_4) and acetic acid were purchased from FUJIFILM Wako Pure Chemical. 4-Bromobenzaldehyde, ethylene glycol, 6,13-pentacenedione and 2-methyl-2-butene were purchased from TCI.

General characterization

^{1}H-NMR (400 MHz) spectra were recorded on a JEOL JNM-ECZ400 spectrometer using TMS as the internal standard. Elemental analysis was carried out using a Yanaco CHN Corder MT-5 at the Elemental Analysis Center, Kyushu University. Powder X-ray diffraction (PXRD) patterns were measured on a Bruker D2 Phaser (Cu-Kα, 30 kV, 10 mA). For making the simulated structure and corresponding simulated PXRD pattern, Materials Studio software was used (Accelrys, Material Studio Release Notes, Release 4.2, Accelrys Software, San Diego 2006). The geometry and unit cell were optimized by Materials Studio Forcite tool (*40*). Thermogravimetric analysis was conducted on a Rigaku Thermo Plus EVO2 under N_2. N_2 adsorption isotherm measurements were carried out on a Bel BELSORP-max. UV–Vis absorption spectra were obtained on a JASCO V-670 spectrophotometer. FT-IR spectra were recorded on a SHIMADZU IRTracer-100 with a Smiths DuraSamplIR II ATR device. Samples were activated at 373 K under vacuum for 12 h prior to the measurements.

Sample preparation

PDBA was prepared according to our previously reported method (*29*).

Scheme 2. Synthetic route of PDBA (4,4'-(pentacene-6,13-diyl)dibenzoic acid)

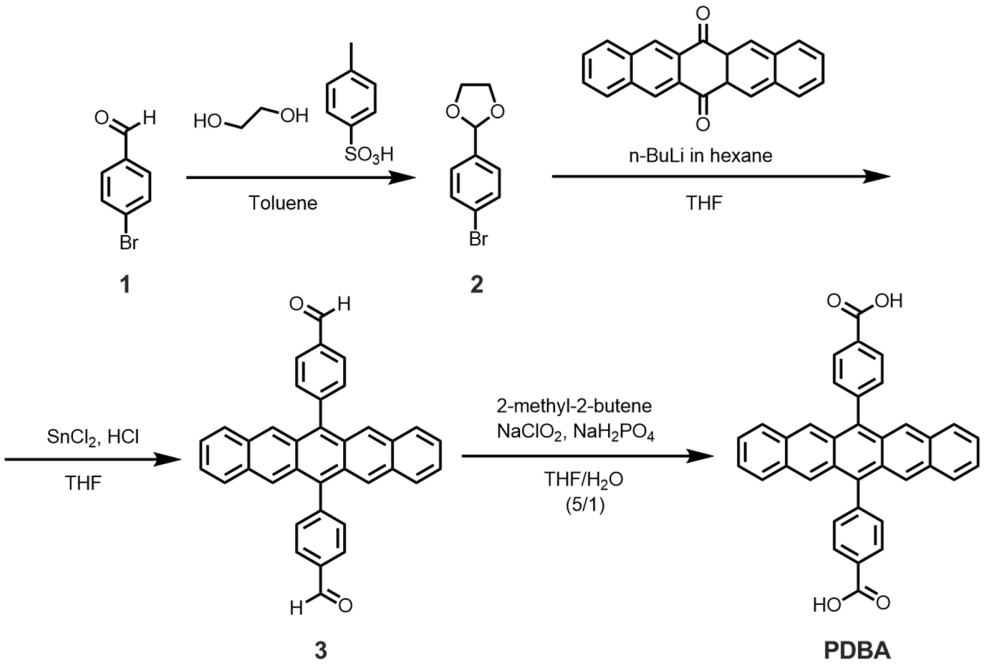

Synthesis of 2-(4-bromophenyl)-1,3-dioxolane (2)

60 mL of a toluene solution of 4-Bromobenzaldehyde (5.0 g, 27 mmol), ethylene glycol (4.3 g, 54 mmol) and *p*-toluene sulfonic acid (0.17 g, 0.90 mmol) was refluxed with a Dean-Stark trap for 8 h. The solution was neutralized with 50 mL K_2CO_3 aqueous solution, then extracted with ethyl acetate (3×50 mL). The organic layer was dehydrated by Na_2SO_4, filtrated and dried under reduced pressure. The orange crude oil was purified using silica gel column chromatography (chloroform/hexane = 1/1), giving a compound **2** as yellow oil. Yield: 5.24 g (85 %).

^{1}H-NMR (400 MHz, DMSO-*d*$_6$, TMS): δ = 7.57-7.64 (d, 2H), 7.35-7.45 (d, 2H), 5.73 (s, 1H), 3.90-4.08 (m, 4H)

Synthesis of 4,4'-(pentacene-6,13-diyl)dibenzaldehyde (3)

n-Butyl lithium in hexane (2.5 M, 6.0 mL, 15 mmol) was dropped to a solution of **2** (3 g, 13.1 mmol) in dry THF (120 mL) at -78 ˚C under N_2 atmosphere. A 20 mL THF solution of 6,13-pentacenedione (1.24 g, 4.0 mmol) was added after stirring for 1 h at -78 ˚C. The reaction was warmed to room temperature and stirred for 24 h. A saturated aqueous NH_4Cl (150 mL) was added to quench the reaction. The mixture was filtered and dried under vacuum. The dark-red oil-like crude was dissolved in 30 mL THF, and added $SnCl_2 \cdot 2H_2O$ (4.2 g, 22 mmol) and 9 mL conc. HCl. To avoid the light exposure, the reaction mixture was covered by an aluminum foil and stirred at room temperature for 24 h. The resulting solution was added 150 mL H_2O and extracted with chloroform (3×100 mL). The organic layer was dehydrated by Na_2SO_4, filtrated and dried under vacuum. Silica gel column chromatography (chloroform/hexane = 1 : 1) gave **3** as a dark purple powder. Yield: 1.61 g (82 %).

^{1}H-NMR (400 MHz, DMSO-d_6, TMS): δ = 10.32 (s, 2H), 8.32 (t, 4H), 8.25(s, 4H), 7.90–7.95 (d, 4H), 7.84–7.88 (m, 4H), 7.31-7.35 (m, 4H).

Synthesis of 4,4'-(pentacene-6,13-diyl)dibenzoic acid (PDBA)

3 (1.61 g, 3.31 mmol) and 2-methyl-2-butene (35 mL, 331 mmol) were dissolved in THF (200 mL) at 0 °C under Ar atmosphere. $NaClO_2$ (1.2 g, 13.2 mmol) and NaH_2PO_4 (2.50 g, 20.9 mmol) in H_2O (40 mL) was added to the suspension and stirred for 3 h. The reaction was slowly warmed to room temperature and stirred for 24 h under dark. After removing THF under reduced pressure, the residue was diluted with water and washed with chloroform and methanol, giving compound PDBA as a dark purple powder. Yield: 1.05 g (65 %)

^{1}H-NMR (400 MHz, DMSO-d_6, TMS): δ = 8.32-8.37 (d, 4H), 8.25 (s, 4H), 7.85-7.88 (q, 4H), 7.78-7.82 (d, 4H). MS (MALDI-TOF-MS): m/z [M+] calculated $C_{36}H_{22}O_4$, 518.57; found 518.33. Elemental analysis for $C_{36}H_{22}O_4 \cdot 2H_2O$: calculated (%) H 4.73, C 77.97, N 0.00; found (%) H 4.92, C 77.90, N 0.13.

Synthesis of Pn-MOF

$ZrCl_4$ (9 mg, 0.0385 mmol) and acetic acid (220 μL, 3.85 mmol) in 2.26 mL of DMF were ultrasonically dissolved in a 6 mL screw vial. After stirring for 6 h at room temperature, PDBA (20 mg, 0.0385 mmol) was added and the mixture was ultrasonicated again. The obtained purple solution was degassed by freeze-pump-thaw for 2 times in a 10 mL ampule and flame-sealed under vacuum. The degassed sample was wrapped with aluminum foil to minimize light exposure and kept in an oven at 403 K for 48 h. The mixture was cooled to room temperature over 72 h, filtered and soaked in methanol for 12 h. After removing the solvent by filtration and drying for 5 h at 323 K, dark green powder was obtained.

TAS measurement

The fs-TAS and ns-TAS experiments were performed using home-built pump-probe setups. A Ti:sapphire regenerative amplifier (Spectra-Physics, Spitfire Ace) was utilized as the light source, (pulse duration: 120 fs, repetition rate: 1 kHz, pulse energy: 4 mJ/pulse, central wavelength: 800 nm), seeded by a Ti:sapphire femtosecond mode-locked oscillator (Spectra-Physics, Tsunami) with a pulse duration of 120 fs, a repetition rate of 80 MHz, and a pulse energy of 10 nJ/pulse. For fs-TAS, one of the outputs from the amplifier was directed towards an optical parametric amplifier (Light Conversion, TOPAS), where the output wavelength was tuned to 600 nm for use as the pump pulse. The other output was focused on a sapphire crystal (3 mm thickness), generating white light in the 450-750 nm range for use as the probe pulse. For ns-TAS, output pulses from an optical parametric oscillator (Light Conversion, NT242, central wavelength: 600 nm, pulse duration: 3 ns) using the THG of a Nd:YAG laser as the excitation pulse. was utilized as a pump pulse. The magic angle (~54.7 deg.) was adopted between the pump and probe polarizations. The probe pulse that passed through the sample was dispersed by a polychromator (JASCO, CT-10, 300 grooves/500 nm) and detected by a multichannel detection system with a CMOS sensor (UNISOKU, USP-PSMM-NP). The Pn-MOF sample was enclosed between

quartz glass plates under an inert gas atmosphere. The TAS measurements were conducted in a semi-transparent position on the Pn-MOF sample.

Time-resolved CWEPR and pulsed EPR measurements

Time-resolved EPR measurements were carried out at room temperature using an X-band (9.682 GHz in the CWEPR and 9.589 GHz in the pulsed EPR) CW/FT EPR spectrometer (ELEXSYS II E580) with a dielectric resonator employing a quadrature detection. Samples were photoexcited by the second harmonics (532 nm) of a Nd:YAG laser (Continuum, Minilite II, fwhm ∼5 ns). A laser depolarizer (SIGMA KOKI, DEQ 1N) was placed between the laser exit and the microwave cavity. Repetition rate and pulse energy were 10 Hz, and 1 mJ/pulse, respectively. The CW-TREPR spectra were obtained by employing a transient mode in the Bruker Elexsys spectrometer. The TREPR signals were directly amplified by a video amplifier using a control program (Xepr) for a digitizer of SpecJet-II. The spin echo measurements in Fig. 5 were performed by using PatternJet-II controlled by the Xepr program. Pulse sequence of the Hahn echo detection (laser–τ_{delay}–$\pi/2$–τ_{echo}–π–τ_{echo}–echo) was employed in the pulse-EPR measurements. The power of microwave pulse was set to maximize the intensity of the spin echo signal of oxidized pentacene species (Fig. S6) observed in the absence of the laser irradiations following the CWTREPR measurement. In this the pulse durations were x = 16 ns and t_2 = 32 ns, respectively. The echo detected field sweep measurements of the triplet pairs were performed by using τ_{delay} = 1.1 μs, τ_{echo} = 200 ns, x = 8 ns and t_2 = 16 ns, and the magnetic field was varied. Transient nutation measurements were performed by varying x from 0 to 400 ns.

Pn-MOF was put into 2 mm capillaries, with or without paraffin. The capillaries were degassed at room temperature with an oil pump and sealed with a flame.

From Scheme 1, we computed time-development of the singlet, triplet and quintet characters for the different exciton-pair conformations together with the J values using coupled stochastic-Liouville equations, as reported previously (*17, 41*). Details of the applied parameters for the multiexciton conformations, the kinetics are listed in Table S1 and S2 to compute the CW-TREPR data and the pulsed EPR data, respectively. The singlet, triplet and quintet diagonal terms in density matrix elements were used to obtain delay time dependences of the excitons (Fig. 4C) of ρ_{SS}^{TT1}, ρ_{SS}^{TT2}, $\rho_{m_S m_S}^{TT1}$, $\rho_{m_S m_S}^{TT2}$, ρ_{mm}^{T1S0}, ρ_{SS}^{T+T}, ρ_{mm}^{T+T} and $\rho_{m_S m_S}^{T+T}$ where m (= +1, 0, -1) represents the quantum number of the triplet sublevels. From scheme 1, the following relations were used: ${}^5TT_1 = \sum_{m_S} \rho_{m_S m_S}^{TT1}$, ${}^5TT_2 = \sum_{m_S} \rho_{m_S m_S}^{TT2}$, ${}^3T_1S_0 = \sum_m \rho_{mm}^{T1S0}$, ${}^1TT_1 = \rho_{SS}^{TT1}$, ${}^1TT_2 = \rho_{SS}^{TT2}$, SCTP = $\rho_{SS}^{T+T} + \sum_m \rho_{mm}^{T+T} + \sum_{m_S} \rho_{m_S m_S}^{T+T}$ (*17, 41*).

References

1. F. Arute *et al.*, Quantum supremacy using a programmable superconducting processor. *Nature* **574**, 505-510 (2019).
2. T. D. Ladd *et al.*, Quantum computers. *Nature* **464**, 45-53 (2010).
3. M. K. Bhaskar *et al.*, Experimental demonstration of memory-enhanced quantum communication. *Nature* **580**, 60-64 (2020).
4. S. Muralidharan *et al.*, Optimal architectures for long distance quantum communication. *Sci. Rep.* **6**, 20463 (2016).
5. C. L. Degen, F. Reinhard, P. Cappellaro, Quantum sensing. *Rev. Mod. Phys.* **89**, (2017).

6. X. Guo *et al.*, Distributed quantum sensing in a continuous-variable entangled network. *Nat. Phys.* **16**, 281-284 (2019).
7. J. R. Maze *et al.*, Nanoscale magnetic sensing with an individual electronic spin in diamond. *Nature* **455**, 644-647 (2008).
8. J. M. Zadrozny, A. T. Gallagher, T. D. Harris, D. E. Freedman, A Porous Array of Clock Qubits. *J. Am. Chem. Soc.* **139**, 7089-7094 (2017).
9. S. von Kugelgen *et al.*, Spectral Addressability in a Modular Two Qubit System. *J. Am. Chem. Soc.* **143**, 8069-8077 (2021).
10. M. R. Wasielewski *et al.*, Exploiting chemistry and molecular systems for quantum information science. *Nat. Rev. Chem.* **4**, 490-504 (2020).
11. S. L. Bayliss *et al.*, Optically addressable molecular spins for quantum information processing. *Science* **370**, 1309–1312 (2020).
12. Y. Qiu *et al.*, Optical Spin Polarization of a Narrow-Linewidth Electron-Spin Qubit in a Chromophore/Stable-Radical System. *Angew. Chem. Int. Ed.* **62**, e202214668 (2023).
13. L. R. Weiss *et al.*, Strongly exchange-coupled triplet pairs in an organic semiconductor. *Nat. Phys.* **13**, 176-181 (2016).
14. R. M. Jacobberger, Y. Qiu, M. L. Williams, M. D. Krzyaniak, M. R. Wasielewski, Using Molecular Design to Enhance the Coherence Time of Quintet Multiexcitons Generated by Singlet Fission in Single Crystals. *J. Am. Chem. Soc.* **144**, 2276-2283 (2022).
15. R. D. Dill, K. E. Smyser, B. K. Rugg, N. H. Damrauer, J. D. Eaves, Entangled spin-polarized excitons from singlet fission in a rigid dimer. *Nat. Commun.* **14**, 1180 (2023).
16. K. E. Smyser, J. D. Eaves, Singlet fission for quantum information and quantum computing: the parallel JDE model. *Sci. Rep.* **10**, 18480 (2020).
17. Y. Kobori, M. Fuki, S. Nakamura, T. Hasobe, Geometries and Terahertz Motions Driving Quintet Multiexcitons and Ultimate Triplet-Triplet Dissociations via the Intramolecular Singlet Fissions. *J. Phys. Chem. B* **124**, 9411-9419 (2020).
18. M. I. Collins, D. R. McCamey, M. J. Y. Tayebjee, Fluctuating exchange interactions enable quintet multiexciton formation in singlet fission. *J. Chem. Phys.* **151**, 164104 (2019).
19. S. Matsuda, S. Oyama, Y. Kobori, Electron spin polarization generated by transport of singlet and quintet multiexcitons to spin-correlated triplet pairs during singlet fissions. *Chem. Sci.* **11**, 2934-2942 (2020).
20. M. Einzinger *et al.*, Sensitization of silicon by singlet exciton fission in tetracene. *Nature* **571**, 90-94 (2019).
21. K. Miyata, F. S. Conrad-Burton, F. L. Geyer, X. Y. Zhu, Triplet Pair States in Singlet Fission. *Chem. Rev.* **119**, 4261-4292 (2019).
22. M. B. Smith, J. Michl, Singlet Fission. *Chem. Rev.* **110**, 6891−6936 (2010).
23. S. Kitagawa, R. Kitaura, S. Noro, Functional porous coordination polymers. *Angew. Chem. Int. Ed.* **43**, 2334-2375 (2004).
24. M. C. So, G. P. Wiederrecht, J. E. Mondloch, J. T. Hupp, O. K. Farha, Metal−organic framework materials for light-harvesting and energy transfer. *Chem. Comm.* **51**, 3501-3510 (2015).
25. B. Joarder *et al.*, Near-Infrared-to-Visible Photon Upconversion by Introducing an S−T Absorption Sensitizer into a Metal-Organic Framework. *ChemNanoMat* **6**, 916-919 (2020).
26. R. Haldar *et al.*, Interplay of structural dynamics and electronic effects in an engineered assembly of pentacene in a metal–organic framework. *Chem. Sci.* **12**, 4477-4483 (2021).
27. S. Fujiwara *et al.*, Triplet Dynamic Nuclear Polarization of Guest Molecules through Induced Fit in a Flexible Metal–Organic Framework. *Angew. Chem. Int. Ed.* **61**, e202115792 (2022).

28. O. M. Yaghi *et al.*, Reticular synthesis and the design of new materials. *Nature* **423**, 705-714 (2003).
29. S. Fujiwara *et al.*, Dynamic Nuclear Polarization of Metal-Organic Frameworks Using Photoexcited Triplet Electrons. *J. Am. Chem. Soc.* **140**, 15606-15610 (2018).
30. J. H. Cavka *et al.*, A New Zirconium Inorganic Building Brick Forming Metal Organic Frameworks with Exceptional Stability. *J. Am. Chem. Soc.* **130**, 13850-13851 (2008).
31. H. Sakai *et al.*, Multiexciton Dynamics Depending on Intramolecular Orientations in Pentacene Dimers: Recombination and Dissociation of Correlated Triplet Pairs. *J. Phys. Chem. Lett.* **9**, 3354-3360 (2018).
32. S. N. Sanders *et al.*, Quantitative Intramolecular Singlet Fission in Bipentacenes. *J. Am. Chem. Soc.* **137**, 8965-8972 (2015).
33. B. J. Walker, A. J. Musser, D. Beljonne, R. H. Friend, Singlet exciton fission in solution. *Nat. Chem.* **5**, 1019-1024 (2013).
34. Y. Kawashima *et al.*, Singlet fission as a polarized spin generator for dynamic nuclear polarization. *Nat. Commun.* **14**, 1056 (2023).
35. Y. Y. Pan *et al.*, Computational investigation on the large energy gap between the triplet excited-states in acenes. *RSC Adv.* **7**, 26697-26703 (2017).
36. J. Perego *et al.*, Highly luminescent scintillating hetero-ligand MOF nanocrystals with engineered Stokes shift for photonic applications. *Nat. Commun.* **13**, 3504 (2022).
37. M. A. Ali *et al.*, Broad Mid-Infrared Luminescence in a Metal-Organic Framework Glass. *ACS Omega* **4**, 12081-12087 (2019).
38. Sanders, S. N. *et al.*, Quantitative intramolecular singlet fission in bipentacenes. *J. Am. Chem. Soc.* **137**, 8965–8972 (2015).
39. Andrew J. Musser, Matz Liebel, Christoph Schnedermann, Torsten Wende, Tom B. Kehoe, Akshay Rao, Philipp Kukura, Evidence for conical intersection dynamics mediating ultrafast singlet exciton fission. *Nat. Phys.* **11**, 352-357 (2015).
40. Accelrys, Material Studio Release Notes, Release 4.2, Accelrys Software, San Diego (2006).
41. S. Nakamura *et al.*, Synergetic Role of Conformational Flexibility and Electronic Coupling for Quantitative Intramolecular Singlet Fission. *J. Phys. Chem. C* **125**, 18287-18296 (2021).
42. M. Gierer, A. v. d. Est, D. Stehlik, Transient EPR of weakly coupled spin-correlated radical pairs in photosynthetic reaction centres: increase spectral resolution from nutation analysis. *Chem. Phys. Lett.* **186**, 238-247 (1991).

Acknowledgments

Funding: This work was partly supported by the JST-FOREST Program (JPMJFR201Y), JSPS KAKENHI (JP20H02713, JP22K19051, JP20K21174, JP20KK0120, JP22K19008), JST SPRING (JPMJSP2136), JST the establishment of university fellowships towards the creation of science technology innovation (JPMJFS2132), JSPS KAKENHI Grant-in-Aid for Transformative Research Areas, “Dynamic Exciton” (JP20H05832), and the Sumitomo Foundation, The Murata Science Foundation, Research Foundation for Opto-Science and Technology, Kyushu University Platform of Inter-/Transdisciplinary Energy Research (Q-PIT) through its “Module-Research Program”

Author contributions: N. Y., Y. K. and K. M. designed the project. A. Y., K. T. and S. F. prepared and characterized the samples, with the input of N. K. and N. Y. T. R., M. S. and K. M. conducted the TAS measurements. A. Y., K. T. and M. F. conducted the EPR

measurements. Y. K. simulated the EPR spectra. A. Y., K. T., Y. K., K. M. and N. Y. wrote the manuscript with contributions from all authors.

Competing interests: All authors declare that they have no competing interests.